

Simulation of Plasma Blobs in Realistic Tokamak Geometry

Rogério Jorge

rogerio.jorge@tecnico.ulisboa.pt

Instituto Superior Técnico, Lisboa, Portugal

October 2014

Abstract

Understanding *Scrape-off Layer* (SOL) turbulence is crucial for the success of the entire magnetic confinement fusion program. It determines the overall confinement and performance of future tokamaks (such as ITER), governs the heat load on the vessel wall, and regulates the impurity dynamics and plasma refueling. In the SOL, the collision frequency is large and the fluctuations are highly anisotropic and occur on scales larger than the ion Larmor radius. This implies that plasma dynamics in the SOL can be investigated with the drift-reduced Braginskii equations. The GBS code numerically integrates these equations, allowing us to model the evolution of the SOL plasma dynamics in 3D, without separation between perturbations and equilibrium. Therefore, GBS is able to model the self-consistent formation of the plasma profiles resulting from the plasma and heat outflowing from the core to the SOL, the cross-field transport arising from turbulence driven by a number of instabilities and parallel losses at the sheaths. In this work the GBS code has been ported to ISTTOK's SOL configuration, asserting the ballooning character of turbulence in the SOL, where the typical gradient length increases at the bad curvature region, and determining the non-linear saturation mechanism through the gradient removal hypothesis. Through a linear code, we determined the influence of the magnetic shear, resistivity and electromagnetic effects in the linear growth rate of the instabilities at play in ISTTOK's SOL. An estimate for the typical pressure gradient length is obtained for the experimental results.

Keywords: plasma physics, magnetic confinement fusion, scrape-off layer, plasma turbulence, ISTTOK, turbulent transport

1. Introduction

In 2012, fossil fuels in Portugal represented 74.9 % of total energy consumption [1]. According to recent reports [2], demand will surpass supply by 2015 if the world's oil depletion rate remains at its 2010 value. Besides being limited resources, fossil fuels pose serious problems of pollution. Hence, it is certain that the need for new sources of energy to replace fossil fuels will certainly become a critical problem in the near future. Nuclear fusion is a promising source of energy to respond to the increasing world energy demand. There is no doubt that this process works, since it is what mainly powers the Sun and the stars, and uncontrolled fusion reactions have been achieved on Earth, such as H-bombs. Nowadays, the biggest challenge is to achieve fusion in a controlled manner, which requires a detailed study on plasma physics. To confine a plasma we need to maintain it in a stable equilibrium state, where the loss of particles and heat in the reactor must be slow enough for it to be self-sustained.

Although nowadays there are several different machines with different geometries and configurations for this purpose, in this thesis we will focus on a specific device designed to achieve nuclear fusion – a tokamak. This is a low pressure gas discharge tube bent into a closed circular shape with a strong toroidal magnetic field, B_ϕ , and a weaker poloidal field, B_θ , containing a high temperature plasma within the torus. We shall study the properties of ISTTOK, a large aspect ratio tokamak with a circular cross-section with a poloidal (graphite) limiter [3]. The limiter controls the parti-

cle movement inside a tokamak, preventing the plasma touching the wall and controlling the plasma-solid interaction. The Debye sheath is formed on the sides of the limiter due to the motion of particles to those locations, where electrons are repelled from the negative electrode, while positive ions are drawn towards it. Around each negative electrode there is thus a sheath of finite thickness containing only positive ions and neutral atoms [4].

One of the major challenges is the extremely complex interaction between the plasma and the device. This requires a profound study of the plasma-surface interaction and the plasma boundary. A key role is played by the Last Closed Flux Surface (LCFS). This is the last flux surface that goes outwards from the main plasma and does not touch a solid surface. In a surface on a region inside the LCFS magnetic lines are closed, while those further out are open. The region radially outboard of the LCFS is called the SOL

In this work we simulate ISTTOK SOL dynamics with the GBS code. This is based on the drift-reduced Braginskii equations and models the SOL plasma turbulence with proper boundary conditions derived from the sheath dynamics [5]. It has been developed with the goal of simulating plasma SOL turbulence by evolving the full profiles of the various quantities with no separation between *perturbations* and *equilibrium* and has been validated against experiments such as the TORPEX device [6]. The issue of plasma *blob* dynamics is not directly addressed. These are structures of enhanced plasma density relative to the background plasma [7],

and they are measured near the edge of magnetized laboratory plasmas such as tokamaks, stellarators, simple magnetized tori and linear devices. In recent years, their study has substantially increased (see e. g. [8] and [9]) as blob dynamics influence important mechanisms such as wall recycling and strength of heat and particle fluxes to the divertor or first wall. Blob dynamics is also influenced by SOL turbulence and the deeper understanding of edge turbulence in the plasma can improve our understanding of blob behavior in ISTTOK and other tokamaks.

In section 2 we derive the set of equations used throughout the thesis and solved by GBS (adimensionalized drift-reduced Braginskii equations) together with the proper boundary and initial conditions. We also present a brief description of the numerical implementation of the code and ISTTOK's geometry. In section 3 the set of equations is linearized and the linear solver is described together with its numerical implementation. The main linear instabilities in the cold ion limit are described: they are Ballooning Modes (BM) and Drift Waves (DW). In order to accurately describe these modes, we assess the influence of each parameter: electron mass, resistivity or plasma β_e , in order to identify the inertial, resistive and ideal branch of BM or the inertial and resistive branch of DW, studying its growth rate as a function of the main SOL parameters. The *gradient removal hypothesis* is also presented; this suggests that turbulence is non-linearly saturated when the radial gradient of the background plasma pressure is of the same order of the radial gradient of the pressure fluctuations [10]. In section 4 we present the simulation results, identifying the non-linear SOL turbulent regimes, comparing with the linear simulation and experimental results. An analysis is done on the dependence of these modes with SOL operational parameters, namely q , magnetic shear \hat{s} , resistivity ν , ion to electron temperature ratio τ and the electromagnetic factor β_e . The role of these parameters is assessed within the linear simulations to different parameters such as $L_P = \frac{P}{\nabla P}$, L_n and L_T . In section 5 the main results are described together with some possible improvements and future developments of this work.

2. Description of the Model and the GBS code

In order to model the turbulence in the edge of a tokamak, one should define a set of equations coherent with the specified regime. To allow the use of a fluid description, the collisionality needs to be high enough so that the plasma is close to thermodynamical equilibrium. This is true in the edge, where the temperatures are much lower than in the core. A widely used model to describe SOL turbulence is the drift reduced model based on the Braginskii equations [11]. As a fluid model, Braginskii equations are based in a closure scheme which assumes that the plasma is collisional and is immersed in a strong magnetic field, which implies $\omega_{e,i}\tau_{e,i} \gg 1$ with $\omega_{e,i} = \frac{qB}{m_{e,i}c}$ the Langmuir frequency and $\tau_{e,i}$ the electron/ion collision times $\tau_e = \frac{3\sqrt{m_e}T_e^{3/2}}{4\sqrt{2\pi}\lambda e^4 Z^2 n_e}$ and $\tau_i = \frac{3\sqrt{m_i}T_i^{3/2}}{4\sqrt{2\pi}\lambda e^4 Z^2 n_i}$ ($\lambda = 24 - \ln\left(\frac{\sqrt{n}}{T_e}\right)$ is the Coulomb logarithm). The Braginskii momentum equation for each

species $s = \{i, e\}$ states

$$m_s n \left(\frac{\partial}{\partial t} + \mathbf{v}_s \right) \mathbf{v}_s = -\nabla p_s \quad (1)$$

$$+ q_s n \left(\mathbf{E} + \frac{\mathbf{v}_s}{c} \times \mathbf{B} \right) - \nabla \cdot \pi_s + \mathbf{R}_s,$$

where we assume a quasi-neutral plasma with electrons and singly charged ions, π is the stress tensor divided into an FLR (finite Larmor radius) part and a viscous part $\pi_s = \pi_s^{\text{FLR}} + \pi_s^{\text{vis}}$ such that $\nabla \cdot \pi_s^{\text{FLR}} = -m_s n \mathbf{v}_{ds} \cdot \nabla \mathbf{v}_{ds} + p_s \left(\nabla \times \frac{\mathbf{b}}{w_{cs}} \right) \cdot \nabla \mathbf{v}_s + \nabla_{\perp} \left[\frac{p_s}{2w_{cs}} \nabla \cdot (\mathbf{b} \times \mathbf{v}_s) \right] + \mathbf{b} \times \nabla \left(\frac{p_s}{2w_{cs}} \nabla_{\perp} \cdot \mathbf{v}_s \right)$ and $\nabla \cdot \pi_s^{\text{vis}} = G_s \kappa - \frac{\nabla G_s}{3} + \mathbf{b} \cdot \nabla G_s \mathbf{b} + G_s \nabla \cdot \mathbf{b}$, where $\mathbf{v}_{ds} = c \mathbf{b} \times \nabla p_s / (q_s n B)$, the field line curvature is $\kappa = \mathbf{b} \cdot \nabla \mathbf{b}$, the stress function $G_s = -3\eta_{0s} [\nabla_{\parallel} v_{\parallel s} \mathbf{b} - \kappa \cdot \mathbf{v} - \nabla \cdot \mathbf{V}_s / 3]$, $\mathbf{b} = \mathbf{B}/B$ and the viscosities $\eta_{0s} = \zeta_s p_s \tau_s$ with τ_s the collisional time for species s and $\zeta_i = 0.96$, $\zeta_e = 0.73$.

The momentum transfer vector \mathbf{R} can be neglected for ions [5] and $\mathbf{R}_e = n \mathbf{b} [e j_{\parallel} / \sigma_{\parallel} - 0.71 \nabla_{\parallel} T_e]$, with $\sigma_{\parallel} = 1.96 n e^2 \tau_e / m_e$ the parallel conductivity and the parallel current $j_{\parallel} = en (V_{\parallel i} - V_{\parallel e})$. The friction in the direction perpendicular to the magnetic field is neglected with respect to the standard Braginskii equations.

The dynamics in these equations range from time scales such as the electron cyclotron frequency $w_{ce} \simeq 10^{11} s^{-1}$ up to the confinement time scale of order 1 s [12]. In order to eliminate fast time scale variations in our system, a drift reduced model is employed using (following [12])

$$\frac{\partial}{\partial t} \approx \mathbf{V}_{E \times B} \cdot \nabla \approx \frac{\rho_s^2}{L_{\perp}^2} \omega_i \ll \omega_i, \quad (2)$$

where typically, at the region of interest, ρ_s is much smaller than the typical equilibrium scale length L_{\perp} and the $\mathbf{E} \times \mathbf{B}$ velocity is $\mathbf{V}_{E \times B} = -\frac{c}{B} \nabla \phi \times \mathbf{b}$ (with ϕ the electric potential). On ISTTOK, $\rho_s / L_p \simeq 0.09$. Thanks to fact that the plasma turbulence takes place on a much bigger spatial scale than the charge unbalancing, namely that $\rho_s \gg \lambda_D$, where $\lambda_D \equiv \sqrt{\frac{T_e}{2\pi e^2 n}}$ is the Debye Length, we can assume a quasi neutral regime $n \equiv n_i = n_e$. Also embedded in the drift ordering is the distinction between dynamics parallel and perpendicular to the magnetic field $\mathbf{V}_s = V_{\parallel s} \mathbf{b} + \mathbf{V}_{\perp}$, where the turbulence is essentially aligned with the field lines, which implies $|\nabla_{\parallel}| \ll |\nabla_{\perp}|$.

The full system of drift-reduced Braginskii equations is derived and presented in [12]. This is a closed set of equations that describes the dynamics of plasma density, vorticity, electron and ion parallel velocities and electron and ion temperatures. In order to summarize them in a straightforward numerical form we introduce the curvature operator $C(f) = \frac{B}{2} (\nabla \times \frac{\mathbf{b}}{B}) \cdot \nabla f$, the Poisson brackets operator $[\phi, f] = \mathbf{b} \cdot (\nabla \phi \times \nabla f)$, the adimensionalized resistivity $\nu = \frac{e^2 n R}{m_i \sigma_{\parallel} c_{s0}}$, the ion to electron temperature ratio $\tau = \frac{T_{i0}}{T_{e0}}$, the reference ion sound speed $c_{s0} = \sqrt{\frac{T_{e0}}{m_i}}$ and the plasma parameter $\beta = \frac{n_0 T_{e0}}{\frac{B^2}{8\pi}}$.

With the definitions above, the system of equations are solved in a normalized form by GBS with the stan-

standard gyro-Bohm normalization (with ρ_s and c_s). We normalize n to the reference density n_0 , T_e and T_i to the reference temperatures T_{e0} and T_{i0} , ϕ to $\frac{T_{e0}}{e}$, $V_{\parallel e}$ and $V_{\parallel i}$ to c_{s0} (and c_s to c_{s0}), ψ to $\frac{\beta c m_i c_{s0}}{2e}$ and time t to $\frac{R}{c_{s0}}$ where R is the major radius. Lengths in the perpendicular direction are normalized to $\rho_{s0} = \frac{c_{s0}}{w_i}$ and in the parallel direction to R . This yields the system

$$\begin{aligned} \frac{\partial n}{\partial t} = & -\frac{R}{B\rho_{s0}} [\phi, n] - \nabla_{\parallel} (nV_{\parallel e}) \\ & + \frac{2n}{B} \left[C(T_e - \phi) + \frac{T_e}{n} C(n) \right], \end{aligned} \quad (3)$$

$$\begin{aligned} \frac{\partial \Omega}{\partial t} = & -\frac{R}{B\rho_{s0}} [\phi, \Omega] - V_{\parallel i} \nabla_{\parallel} \Omega + B^2 \nabla_{\parallel} j_{\parallel} \\ & + B^2 j_{\parallel} \nabla_{\parallel} \log(n) + 2BC(T_e + \tau T_i) \\ & + 2BC(n) \frac{T_e + \tau T_i}{n} + \frac{B}{3n} C(G_i), \end{aligned} \quad (4)$$

$$\begin{aligned} \frac{\partial U_{\parallel e}}{\partial t} = & -\frac{R}{B\rho_{s0}} \frac{m_e}{m_i} ([\phi, V_{\parallel e}] + V_{\parallel e} \nabla_{\parallel} V_{\parallel e}) \\ & - (1.71 \nabla_{\parallel} + \nabla_{\parallel} \log(n)) T_e \\ & + \nabla_{\parallel} \phi - \frac{2}{3} \nabla_{\parallel} G_e + \nu j_{\parallel}, \end{aligned} \quad (5)$$

$$\begin{aligned} \frac{\partial V_{\parallel i}}{\partial t} = & -\frac{R}{B\rho_{s0}} [\phi, V_{\parallel i}] - V_{\parallel i} \nabla_{\parallel} V_{\parallel i} - \frac{2}{3} \nabla_{\parallel} G_i \\ & - (\nabla_{\parallel} + \nabla_{\parallel} \log(n)) (T_e + \tau T_i), \end{aligned} \quad (6)$$

$$\begin{aligned} \frac{\partial T_e}{\partial t} = & -\frac{R}{B\rho_{s0}} [\phi, T_e] - V_{\parallel e} \nabla_{\parallel} T_e - \frac{2}{3} T_e \nabla_{\parallel} V_{\parallel e} \\ & + \frac{2}{3} T_e 0.71 (\nabla_{\parallel} + \nabla_{\parallel} \log(n)) j_{\parallel} \\ & + \frac{4}{3} \frac{T_e}{B} \left(\frac{7}{2} C(T_e) + \frac{T_e}{n} C(n) - C(\phi) \right), \end{aligned} \quad (7)$$

$$\begin{aligned} \frac{\partial T_i}{\partial t} = & -\frac{R}{B\rho_{s0}} [\phi, T_i] - V_{\parallel i} \nabla_{\parallel} T_i + \frac{4}{3} \frac{T_e^2}{B} \frac{C(n)}{n} \\ & + \frac{4}{3} \frac{T_e}{B} C \left(T_e + \tau \frac{5}{2} T_i - \phi \right) \\ & + \frac{2}{3} T_i (j_{\parallel} \nabla_{\parallel} \log(n) - \nabla_{\parallel} V_{\parallel e}), \end{aligned} \quad (8)$$

where $\Omega = \omega + \tau \nabla_{\perp}^2 T_i$, $U_{\parallel e} = \frac{m_e}{m_i} V_{\parallel e} + \frac{\beta e}{2} \psi$, $\nabla_{\perp}^2 \psi = n(V_{\parallel i} - V_{\parallel e})$, $\nabla_{\perp}^2 \phi = w$ and $\mathcal{D}_A A \equiv \mathcal{D}_A(A)$. For a more detailed derivation see [5]. The model is composed by the continuity equation, the vorticity equation, Ampere's law, the equation for the ion and electron parallel motion and the equation for the ion and electron temperatures. For each field A we add a source term

$S_A = A_f e^{-\frac{(x-x_s)^2}{\sigma_s^2}}$ where x_s represents the radial position of the source, A_f its strength and σ_s its width and a diffusion operator \mathcal{D}_A for numerical purposes. Its full form depends on the quantity A . As an example, for the electron temperature term, the diffusion coefficient

$\mathcal{D}_{T_e}^{\parallel}$ is derived from the term $\nabla \cdot (\chi_{\parallel e} \nabla_{\parallel} T_e)$ supposing $\chi_{\parallel e}$ constant.

The system of equations (3) - (8) is stated for a general layout of equilibrium magnetic field but we shall port it to ISTTOK's geometry, for which we expect a poloidal symmetry in the simulation results (as opposed to a toroidal limiter that provides toroidal symmetry). We also consider an $s-\alpha$ geometry (where operators are computed in the large aspect ratio limit $\epsilon = a/R \rightarrow 0$).

A right handed coordinate system $[y, x, z]$ is used, where x is the flux coordinate and corresponds to the radial direction (since we work in a circular magnetic flux surface), z is a coordinate parallel to the total magnetic field \mathbf{B} (where $z = 0$ and $z = 2\pi$ corresponds to the location of the limiter) and y is the coordinate perpendicular to both x and z . In the large aspect ratio limit, the plane (x, y) coincides with the poloidal plane, which implies $y = a\theta$, where $0 < \theta < 2\pi$ is the poloidal angle and $0 < z < 2\pi$.

In this geometry, the previously defined operators take the form $[f, g] = \partial_y f \partial_x g - \partial_x f \partial_y g$, $C(f) = \sin \theta \partial_x f + \cos \theta \partial_y f$, $\nabla_{\perp}^2 f = \partial_x^2 f + \partial_y^2 f$ and $\nabla_{\parallel} f = \partial_z f + \frac{R\beta}{2} [\psi, f]$. In this system, the pitch of the field line varies radially in the presence of magnetic shear. This effect is studied in section 3.

In table 1 we state the code input and typical parameters for ISTTOK in GBS units (lengths normalized to ρ_s).

Major Radius (R)	503.7
Minor Radius (a)	93.08
SOL width	16.43
β	2.577×10^{-5}
L_y	584.8
ν	1.137×10^{-3}
m_e/m_i	0.00055
q	8

Table 1: Code input parameters for ISTTOK in GBS units [13] (1 GBS unit $\simeq 1$ mm).

In order to reduce the computational cost of the simulations, we take advantage of the fact that turbulence is mostly aligned in the direction parallel to the field. For this purpose, we choose N_y and N_z in such a way that the discretization points fall on the field lines, *i.e.* we impose $\Delta_j = \frac{N_y}{N_z q} \in \mathbb{N}$, which allows the use of a low resolution in the toroidal direction. The parallel derivative can then be approximated as $(\mathbf{b} \cdot \nabla) A_{i,j,k} \simeq \frac{1}{2\Delta z} (A_{i,j+\Delta j,k} - A_{i,j-\Delta j,k})$. In the x and y directions a standard centered finite difference scheme is used with $\frac{\partial A}{\partial x} \Big|_{i,j,k} \simeq \frac{1}{2\Delta x} (A_{i+1,j,k} - A_{i-1,j,k})$, except the Poisson brackets, which are discretized according to the Arakawa scheme. A second order centered finite difference scheme is used on the Laplacian operator and a fourth order Runge-Kutta scheme is used for the time stepping. In order to ensure the positivity of n , T_e and T_i , Eqs. (3) to (8) are rewritten in terms of $\theta_n = \log n$, $t_e = \log T_e$ and $t_i = \log T_i$.

The parallelization scheme is done with a standard MPI domain decomposition. The total number of processes is $N_p \equiv N_{Px} N_{Pz}$, where the physical domain

in x and z is divided as equally as possible into N_{Px} and N_{Pz} parts. With the addition of one ghost cell to the left and to the right, each array representing the physical quantity $A(x, y, z)$ will have a size of $\left(\frac{N_x}{N_{Px}} + 2\right)(N_y + 2)\left(\frac{N_z}{N_{Pz}} + 2\right)$ elements in each process. For more details we refer the reader to [5].

An extensive derivation of the boundary conditions at the magnetic presheath entrance is presented in [14]. GBS allows the choice between Neumann and Dirichlet boundary conditions for all the fields but for the parallel electron and ion velocities, Bohm's boundary conditions are implemented. These are derived using a detailed kinetic treatment of the electron dynamics in the sheath region (see [15]). So at the sheath, particularly at $z = 0$ and at $z = 2\pi$ (at the limiter), we use $V_{||e_s} = \pm\sqrt{T_e}e^{\Lambda - \frac{\phi}{T_e}}$ and $V_{||i_s} = \pm\sqrt{T_e}\sqrt{1 + \tau\frac{T_i}{T_e}}$.

3. Analysis of ISTTOK's SOL turbulent regimes

3.1. Linear Model

We begin with a linear study on the GBS equations. We linearize the system of Eqs. (3) to (8) assuming that the equilibrium n and T can be described as $f = f_{00}\left(1 + \frac{x}{L_f}\right)$ where f_{00} represents the equilibrium value and looking for solutions of the form $e^{\gamma t}$ where γ is the linear growth rate of the mode [16].

The main parameters characterizing the SOL in this linear drift-reduced model are L_n , the typical gradient scale length and $\eta_{e,i} = \frac{L_n}{L_{Te,i}}$ together with the plasma β_e , parallel resistivity ν , magnetic shear \hat{s} , the tokamak major and minor radii R and a and the safety factor q . Despite the apparent simplicity of the mode, it allows us to capture the most important properties of DW (Drift Waves) and BM (Ballooning Modes). It has been shown in non-linear electromagnetic models (both fluid and gyrofluid) in agreement with experimental results that these instabilities typically determine the plasma turbulent dynamics in the SOL (see *e.g.* [17]) so that will be the focus of our studies.

The ∂_y operator is substituted by ik_y and the parallel derivative is calculated directly on the discretized parallel direction z with a finite difference scheme. Therefore, the curvature operator and the Laplacian operator become $C = -2ik_y\left[\cos\frac{z}{q} + \frac{z}{q}\hat{s}\sin\frac{z}{q}\right]$ and $\nabla_{\perp}^2 = -k_{\perp}^2 = -k_y^2\left[1 + \left(\hat{s}\frac{z}{q} - \pi\hat{s}\right)^2\right]$. This reduces our set of linear equations to a one-dimensional eigenvalue problem in the z direction for γ which is solved by the linear code. It discretizes $z = [0, L_z]$ with N_z points with a grid distance between each point $\Delta z \equiv z_{i+1} - z_i = \frac{L_z}{N_z - 1}$ and $z_i = (i - 1)\Delta z$ for the quantities n , ϕ , T_e and T_i . As in GBS, we compute a different grid for ψ and $V_{||i}$ having $N_z - 1$ points with the same grid distance Δz and $y_z = (i - 1/2)\Delta y$. We denote the first as the unshifted grid and the last as the shifted grid. We refer the reader to [16] for a detailed description of the numerics.

A number of instabilities are described by the system of Eqs. (9) - (14). We shall focus on the major properties of Drift Waves (DW) and Ballooning Modes (BM) whose linear properties have been extensively studied

(see for example [18], [19] and [17]).

With $\Omega = \omega + \tau\nabla_{\perp}^2 T_i$ and $U_{||e} = \frac{m_e}{m_i}V_{||e} + \frac{\beta_e}{2}\psi$ the linear system is given by

$$\gamma\frac{n}{n_{00}} = +\frac{2}{B}C\left(T_e + \frac{T_{e00}}{n_{00}}n - \phi\right) + \frac{R}{L_n}ik_y\phi - \nabla_{||}V_{||e}, \quad (9)$$

$$\gamma\Omega = +2B\left[C(T_e) + \frac{T_{e00}}{n_{00}}C(n)\right] + 2B\tau\left[C(T_i) + \frac{T_{i00}}{n_{00}}C(n)\right] + \frac{B^2}{T_{e00}}\nabla_{||}j_{||}, \quad (10)$$

$$\gamma U_{||e} = -\nabla_{||}\left(1.71T_e - \frac{T_{e00}}{n_{00}}n\right) + \nabla_{||}\phi + \nu j_{||}, \quad (11)$$

$$\gamma V_{||i} = -\nabla_{||}(T_e + \tau T_i) - \frac{T_{e00} + \tau T_{i00}}{n_{00}}\nabla_{||}n, \quad (12)$$

$$\gamma\frac{T_e}{T_{e00}} = \frac{R}{LT_e}ik_y\phi + \frac{4}{3B}C\left(\frac{7}{2}T_e + \frac{T_{e00}}{n_{00}}n - \phi\right) + \frac{2}{3}0.71\nabla_{||}j_{||} - \frac{2}{3}\nabla_{||}V_{||e}, \quad (13)$$

$$\gamma\frac{T_i}{T_{i00}} = +\frac{4}{3B}C\left(T_e + \frac{T_{e00}}{n_{00}}n - \phi\right) + \frac{R}{LT_i}ik_y\phi - \frac{10\tau}{3B}C(T_i). \quad (14)$$

3.2. Linear instabilities

DWs arise primarily due to the $\mathbf{E} \times \mathbf{B}$ convection of the density profile [12]. In order to model DW within the linear model described in (9) - (14) we linearize the perpendicular gradients, neglect the curvature (ballooning) terms and the coupling with sound waves by considering $k_{||} \ll \gamma$ (therefore neglecting $V_{||i}$ dynamics) [16]. We consider the two branches of the drift wave instability in the cold ion limit, the resistive and the inertial one. The resistive branch of DW (RDW) is characterized by the presence of finite resistivity which brakes the adiabaticity. It is obtained by neglecting electron inertia ($\frac{m_e}{m_i} \rightarrow 0$) and electromagnetic effects ($\beta \rightarrow 0$). In the inertial branch (InDW) the adiabaticity is broken by the presence of finite electron mass, being retrieved by neglecting resistivity ($\nu \rightarrow 0$) and electromagnetic effects.

Ballooning modes (BMs) are driven by an interchange character and the presence of a magnetic field line curvature and plasma pressure gradients, so to model them we neglect the coupling with sound waves, plasma compressibility, parallel flows in the density and temperature equations and the $\nabla_{||}(n + 1.71T_e)$ term in Ohm's law. Here, we consider the 3 branches associated with BM. The resistive branch (RBM) is retrieved neglecting electron inertia and electromagnetic effects, the inertial one (InBM) by neglecting resistivity and electromag-

netic effects and the ideal (IdBM) neglecting electron inertia and resistivity.

3.3. Saturation Mechanism

There are several mechanisms that have been proposed to explain the saturation of linear modes during the non-linear phase (*e.g.* [20] and [21]). In [10], it has been shown that the growth of the Kelvin-Helmholtz instability and the *gradient removal mechanism* play a major role in the SOL through the analysis of the drift-reduced Braginskii equations. The latter dictates that the saturation of the linear mode is due to the non-linear flattening of the driving plasma gradients. Analytical estimates and numerical simulations [10], show that the gradient removal saturation mechanism is the one at play in the typical regime of SOL turbulence when $\sqrt{L_p k_y} < 3$ (the KH-stable parameter regime). This mechanism provides an estimation of L_p as a function of the SOL operational parameters that has a quantitative good agreement with simulation and experimental results [10] and, in normalized units, has the form $L_p = \gamma/k_y$.

The linear code provides the growth rate γ for a given value of k_y and, through a set of values (γ_i, k_{yi}) , we seek the value that yields largest transport choosing the maximum of the ratio γ/k_y . As L_p also depends on the different SOL operational parameters, we obtain a value of L_p that satisfies $L_p = \gamma/k_y$ through Muller's method maintaining all other parameters fixed.

3.4. Non-linear Analysis Techniques

We will now turn to the non-linear tests performed on the simulations to accurately assess the character of the turbulent modes. With the definition of L_p , after averaging over y and z , we seek the decay-like behavior

$$p(x) = p_0 e^{-\frac{x}{L_p}}. \quad (15)$$

Within ISTTOK's geometry, the presence of a poloidal limiter implies not only a poloidal symmetry in our system but that the HFS is located at the poloidal location $\theta = 0$ and the LFS at $\theta = \pi$. As the plasma is highly confined in the HFS it should in principle drive little turbulence across the magnetic field lines and the reverse is true for the LFS. As L_p is a measure of this transport across the magnetic field lines, it should increase in the LFS and decrease at the HFS while being poloidally periodic (which in turn provides a "Gaussian-like" figure for $L_p(y)$). This analysis on L_p is divided in three tests - first obtain an absolute estimate for L_p through a toroidal and poloidal averaging, then estimate the poloidal variation of this value and hence obtaining $L_p(y)$ and finally estimate the toroidal variation and obtain $L_p(z)$ at the HFS and LFS.

We apply a "cross-coherence" technique which asserts the DW character of the domain of interest. Since in this case electrons are close to adiabaticity, the amplitudes of ϕ and n are correlated. To see this, we look to the linear Ohm's law in the isothermal limit $\gamma \left(\frac{m_e}{m_i} V_{\parallel e} + \frac{\beta_e}{2} \psi \right) - \nu J_{\parallel} = \nabla_{\parallel} \left(\phi - \frac{T_{e00}}{n_{00}} n \right)$. In this case, the adiabatic braking terms have the parameters β_e, ν

and $\frac{m_e}{m_i}$, which in the HFS are small comparing with the RHS, where the parallel gradients become dominant. Therefore, we can estimate that $\phi \simeq \frac{T_{e00}}{n_{00}} n + \text{constant}$ and should obtain a clearly correlated plot of $\phi(n)$. At a fixed radial location and at a half distance in the toroidal direction the ϕ and n fluctuations are normalized to their standard deviation. We then evaluate the probability of finding both fluctuations at a certain ordered pair of amplitudes.

Experimentally, the different modes discussed in this section have been observed on ISTTOK (see for example [22]). The HFS and LFS separation has been measured in detail and can be compared with the non-linear and linear results. One of the experimental diagnostics is the frequency spectrum of the floating potential $V_f = V - 3T_e$. As typically observed in the boundary plasma of fusion devices [13], it is found on ISTTOK (Fig. 1) that the lowest frequency part of the spectrum ($f < 30 - 50$ kHz) is nearly independent of the frequency and the high frequency part ($f > 80 - 100$ kHz) shows a power-like decay with indices close to -2 both at LFS and HFS. The transition region shows a slope of -1 . We can then compare the power indices and the overall behavior $\text{FFT}(V_f(\text{HFS})) < \text{FFT}(V_f(\text{LFS}))$ at the high-frequency with the GBS simulation results.

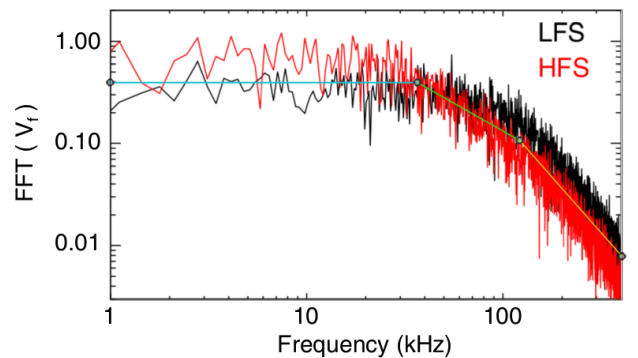


Figure 1: Experimental power-spectrum results performed at ISTTOK (figure taken from [13]). The blue line represents the first low-frequency region, the green line the transition region with a slope of -1 and the yellow one the high frequency region with a slope of -2 .

4. Results

Comparing the SOL parameters that determine the different instability branches in ISTTOK, β has a value of $\simeq 10^{-5}$, whereas $\nu \simeq 10^{-3}$ and $m_e/m_i \simeq 5 \times 10^{-4}$. The small influence of β and \hat{s} (magnetic shear) is confirmed below with the linear code. For this reason, GBS simulations were performed using ISTTOK-like parameters without electromagnetic effects and without magnetic shear. The simulations are performed with the typical ISTTOK's edge value of $q = 8$ for cold and hot ions, containing $(N_x = 64, N_y = 512, N_z = 32)$ grid points in the (x, y, z) directions. The plasma and heat source are located at $x = 15$ with $\sigma_s = 2.5$. Further input parameters are provided in table 1. For a typical simulation, we use 32 cores through the course of 1 week reaching $\simeq 1000$ GBS time units (approximately 5000 CPU hours).

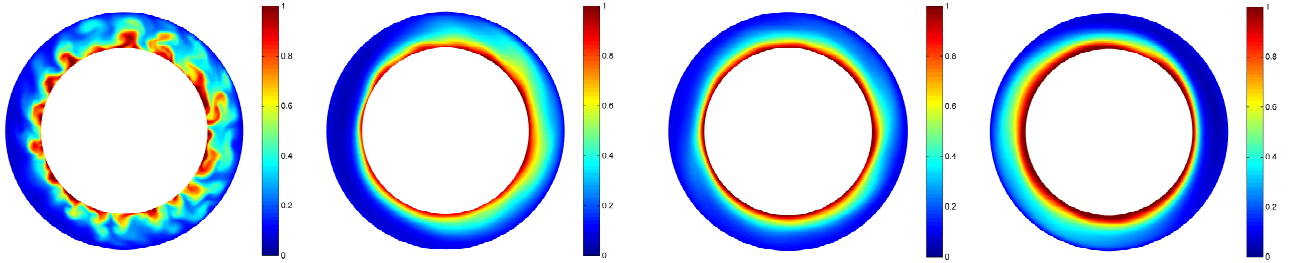


Figure 2: Typical snapshot of GBS simulations at a poloidal plane halfway between the limiter. ($z = N_z/2$) Plots show contours of density at a specific time slice (left) and averaged over the steady-state period (right).

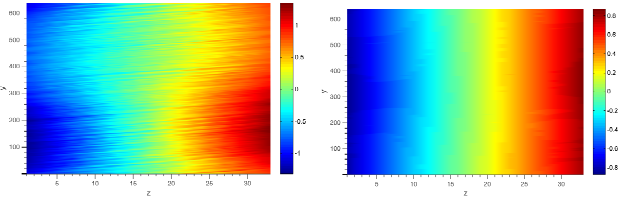


Figure 3: Typical snapshot of GBS simulations at a toroidal plane at $x = 20$ (out of 64 x grid points). Plots show contours of electron (left) and ion (right) parallel velocity averaged over the steady-state period.

In Fig. 2 we represent a typical density snapshot for cold ions in a poloidal plane (as a function of x and y) at halfway between the limiter ($z = \frac{L_z}{2}$) in a turbulent state and the same quantity averaged over the quasi-steady period. The ring shown starts at the radial position of the source and ends at the wall. There is an observed radial fall-off that depends on y , leading to the prediction that $L_p(\text{LFS}) > L_p(\text{HFS})$. In Fig. 3 we look at the ion and electron parallel velocities in the toroidal plane (as a function of y and z) for a cold ion simulation. Since electrons possess small inertia, the averaging is not as clear as in the ion parallel velocity, where we see that ions start at $z = 0$ with velocity equal to $-c_{s0}$ (-1 in our normalization) and end at $z = 2\pi$ with c_{s0} . The value is consistent with the Bohm sheath condition, where it expresses for electrons a limiter value of $\pm c_{s0} e^{\Lambda - \frac{\phi}{T_e}}$. This is why the electron velocity has limiting values beyond 1 and -1 at the boundaries (it also has a dependence on ϕ and T_e).

Simulations were also performed with no DW coupling, where we neglect the diamagnetic term in Ohm's law ($\nabla_{\parallel} (n + 1.71T_e)$), and with no BM coupling, where the interchange terms in the vorticity equation are turned off. In Fig. 4 we see these two simulation results, averaging the density profile over the simulation period. We note that turning off the interchange drive the ballooning character observed before (where $L_p(\text{LFS}) > L_p(\text{HFS})$) is lost.

Simulations with a different value of $q = 4, 6, 10, 12$ and with $\tau = 1, 2$ were also performed with no fundamental difference in the results detailed in this section.

In order to test the dependence $p(x) = p_0 e^{-x/L_p}$ we average the total pressure over y and z and plot the resulting profile in Fig. 5. We identify the exponential decay character right after the source at $x = 15$ until ap-

Figure 4: Snapshot of GBS simulations with no DW (left) and no BM (right) coupling at a poloidal plane halfway between the limiter. Plots show contours of density averaged over the steady-state period.

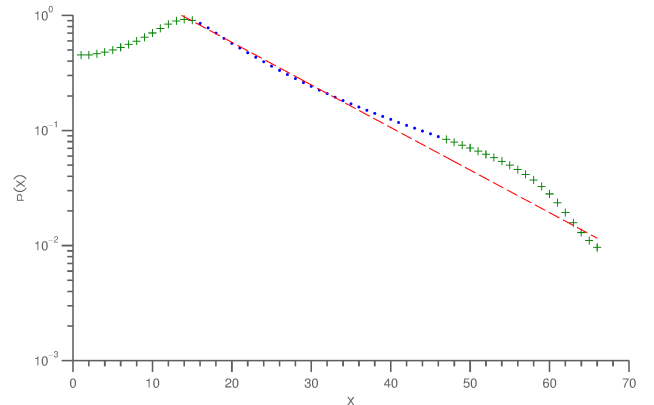


Figure 5: Fit to the expression $p(x) = p_0 e^{-x/L_p}$ for the resulting pressure profile toroidally and poloidally averaged. The logarithmic vertical axes allows the visual separation of the characteristic exponential decays right after the source at $x = 15$ and before the wall. The fit results in a $L_p = 1.1$ cm with a SOL width of 4.6 cm. The green crosses indicate values excluded from the fit.

proximately $x = 50$. This will be the domain where the L_p test will be performed (red dashed lines). After that region the decay possesses a different decay parameter, which is more closely related with the radial boundary conditions than with the turbulence itself. The SOL width in these simulations is of 4.6 cm (50 GBS units) which is 3 cm larger than ISTTOK but, based on simulations with a SOL realistic width of 1.5 cm, L_p scales with the SOL width within the non-linear simulations. These simulations with smaller domain require a much greater value of the diffusion coefficient, which alters significantly the results of the non-linear tests.

The fit on Fig. 5 provides an $L_p = 1.1$ cm, less than a fourth of the whole domain, with a value of the coefficient of determination $R^2 = 0.9937$ ($R^2 = 1 - \frac{\sum_i (y_i - f_i)^2}{\sum_i (y_i - \bar{y})^2}$). The starting and end position where chosen so that R^2 would be the maximum and L_p would not deviate too much. With this result, we can look at the value of L_p for a specific toroidal and poloidal region. In order to describe the fit at a 95 % confidence value we include the error bars that characterize this region. For the variation of $L_p(y)$ with the poloidal angle, we see at Fig. 6 a periodic domain that provides a variation of over 50 %. As we saw in the previous section, one of the addressed instabilities

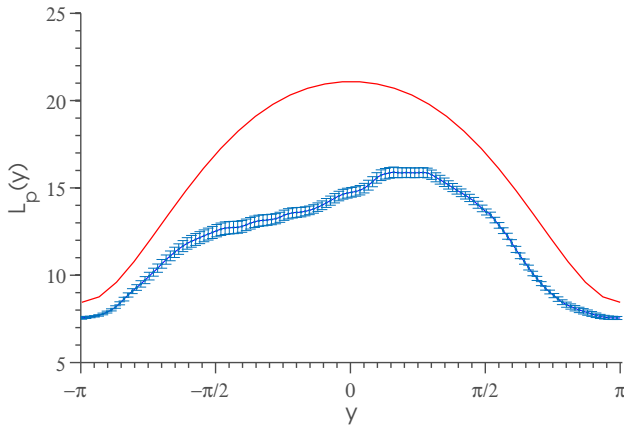


Figure 6: Poloidal variation of L_p from the fit to non-linear simulations (blue) and from the gradient removal hypothesis (red). The vertical axes shows L_p in GBS units, where 1 GBS unit = 0.91 mm.

(BM) has a different character at the LFS (center of the plot) and at the HFS (starting and ending region of the plot) while DW remain with the same characteristics through y .

We can estimate L_p through the gradient removal theory and compare this prediction with the non-linear simulations. First we note that all the non-linear simulations satisfy the inequality $\sqrt{k_y L_p} < 3$, since we obtain a maximum value of $k_y = 0.2$ and even for the maximum $L_p = 16$ at the LFS one has $\sqrt{k_y L_p} \sim 1.8$ and therefore they belong to the regime where the gradient removal mechanism is responsible for the turbulence saturation. In Fig. 6 we show the resulting poloidal variation of L_p provided by the gradient removal hypothesis (together with the linear code). We see a periodic and symmetric figure, with the same behavior as in the non-linear simulations (increasing at the LFS and decreasing at the HFS). As we have seen, the ballooning instability could be the one responsible for this variation at the LFS due to its different character along y .

It is also useful to look at the adimensionalized parameter η_e since it allows the comparison to the experimental results where the actual SOL width scale is not relevant since $\eta = \frac{L_p}{L_T}$ and the common factors of dimensions and units cancel out. In Fig. 7 we show the resulting η_e value through a radial fit of the density and temperature toroidally and poloidally averaged profiles to an exponential behavior like before, and in Fig. 8 we look at the poloidal variation of η_e . An average value of $\eta_e = 0.80$ is obtained through the fit. This value is the one used to compare the experimental results with the non-linear simulations. The value of η_i could also be used, but experimentally only T_e is known with precision at the SOL and through the introduction of a finite τ in GBS we obtain $\eta_i \simeq \eta_e$.

We now study the relative importance of each instability branch described in section 3: RBM, InBM, RDW and InDW. Each instability branch provides a different estimate for L_p . The BM branches provide the ballooning character seen before of $L_p(\text{LFS}) > L_p(\text{HFS})$, while the DW branches provide a constant L_p through all

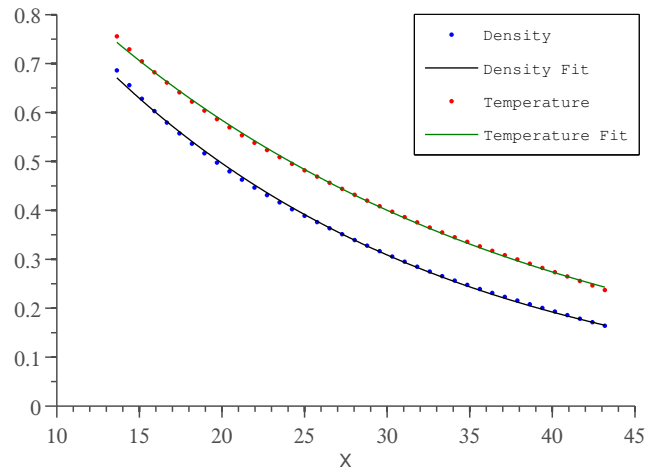


Figure 7: Poloidally and toroidally averaged density and electron temperature profiles fitted to an exponential behavior. The obtained value of $\eta_e = \frac{L_p}{L_{Te}}$ is $\eta_e = 0.80$.

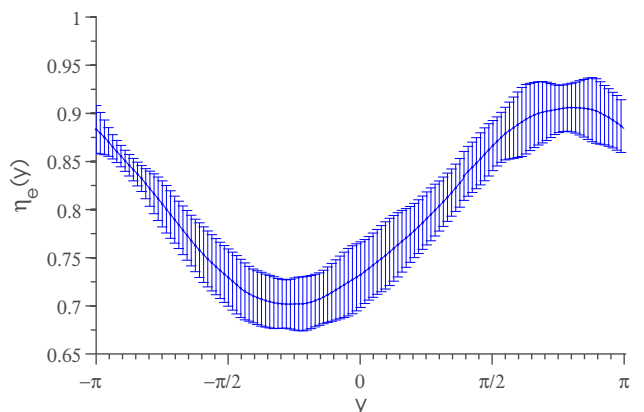


Figure 8: Poloidal variation of η_e from the fit to non-linear simulations.

poloidal angles. This can be seen quantitatively in Fig. 9, where the estimates were performed with the same input parameters as in Fig. 6. We see that the branches that generate the greatest value of L_p are InBM at the LFS and InDW at the HFS. Performing a scan in q , ν , \hat{s} , τ and β_e we shall determine if this constitutes a trend and therefore the turbulence is characteristic of the geometry itself or if the parameters change the fundamental properties of the fluctuations and equilibrium of the plasma profile. The introduction of a finite β_e also leads to the appearance of the Ideal Ballooning Mode (see section 3), whose importance will be assessed.

For the scan analysis we shall look at the growth rate itself, running the linear solver after the determination of L_p with the gradient removal hypothesis, so we can follow previous linear studies in the SOL with the drift-reduced Braginskii equations (such as [16]). It has been seen in [16] that magnetic shear can play a major role in the determination of the growth rate of each instability branch. Since this parameter was not present in the non-linear simulations, we present for each growth rate a scan in \hat{s} and a scan in the poloidal variable y such as

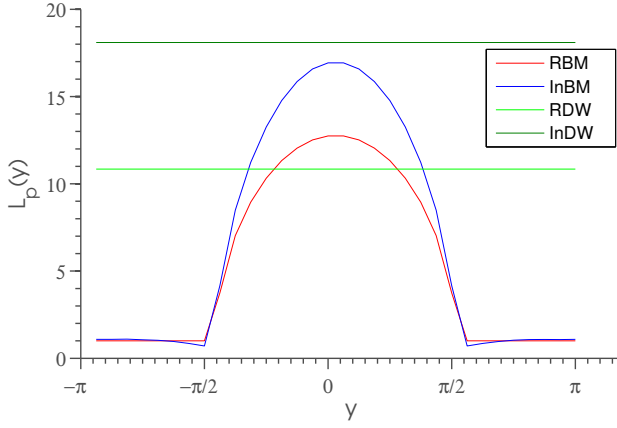


Figure 9: Poloidal variation of L_p for the 4 instability branches provided by the gradient removal hypothesis for ISTTOK-like parameters.

for the L_p analysis, so each y and \hat{s} we determine which branch provides the greatest growth rate γ .

From Fig. 10 we see that, except for values of $\nu < 10^{-3}$, the instability branches that are predicted to play a major role at ISTTOK's SOL remain the same through a scan in τ , q , ν and β_e . It is determined that as τ increases, there is an extension of the InDW region, while for different β_e and q the results stay the same. As ν drops to a value closer to m_e/m_i , the RBM starts to play a role but only in a very small region, negligible for all values of \hat{s} except $\hat{s} = 1.5$. It was also seen that the absolute value of L_p and γ does not alter significantly with \hat{s} . For the case of $\nu < 10^{-3}$, the RBM starts to dominate at the LFS. This shows a strong dependence on this parameter, as even for slight changes on ν the dominant instabilities are different. A non-linear simulation with lower values of resistivity is needed in order to fully assess its influence.

Following [16], the parameter that describes the damping of the mode due to the resistive parallel spread (relevant in the RBM) is σ_R (16) and the one that describes the damping due to the inertial spread is σ_{In} (16). It is also shown that the growth rate increases as σ_R and σ_{In} decreases. If we look at the ratio $\sigma_R/\sigma_{In} = \sqrt{m_e/m_i}/(\nu k_y)$ for ISTTOK (using the typical value of $k_y = 0.2$ obtained from the linear code) we get the value $\simeq 100$ which points to the dominance of the inertial branch (the same analysis may be applied to the drift wave resistive and inertial branch). Note that in ISTTOK $\nu_{ISTTOK} > m_e/m_i$.

$$\sigma_R = \sqrt{\frac{L_p}{2R}} \frac{1}{k_y^2 \nu}, \quad \sigma_{In} = \sqrt{\frac{L_p m_i}{2R m_e}} \frac{1}{k_y} \quad (16)$$

In Fig. 11 we perform the cross-coherence test, looking at a scatter plot between potential and density fluctuations (normalized by their respective standard deviation) for the cold ion simulation, which shows a higher correlated plot at the HFS than at the LFS. As we have seen in section 3, it is an evidence of the DW character of turbulence at the HFS, where the interchange drive is not as relevant. This points to the same results that we have seen through the linear solver (Fig. 10).

The phase shift test provided no concrete results.

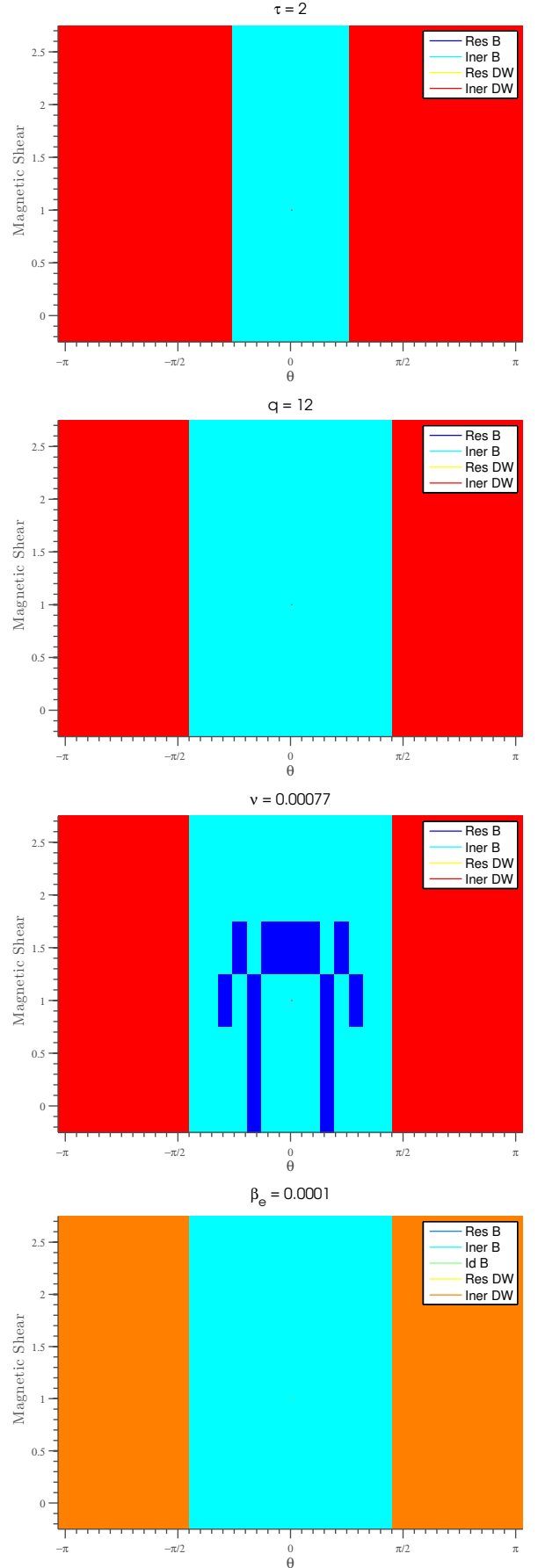


Figure 10: Each figure shows which branch provides the greatest linear growth rate as a function of the poloidal angle and magnetic shear. With a scan on each variable τ , q , ν and β_e the inertial DW and BM are the major predicted branches at play at ISTTOK's SOL.

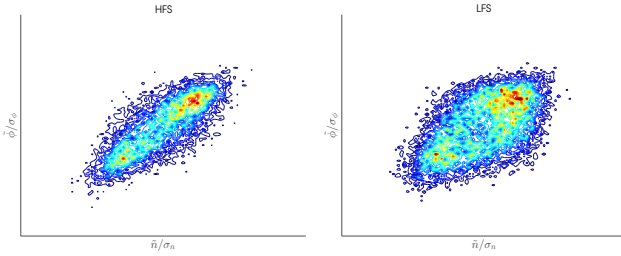


Figure 11: Cross-coherence test at the HFS (left) and LFS (right) (electric potential vs density) for an ISTTOK-like simulation with cold ions.

Lastly, the power-spectrum test is shown in Fig. 12. The non-dependence of the $\text{FFT}(V_f)$ (and also for the $\text{FFT}(N_e)$) with the frequency is clearly observed for $f < 80$ kHz and the power indices for LFS are greater than at the HFS. In ISTTOK [13] the non-dependence for low frequencies has been observed as well as a small difference in the power indices (see Fig. 1).

In order to verify which are characteristic frequencies present we first note that the characteristic time used as a normalization to model the SOL parameters in the GBS code is $\frac{c_s}{R} \simeq 95$ kHz. Looking at the value of $\frac{c_s}{2\pi R}$, which can be thought as the characteristic *angular velocity* of the particles around the torus in the SOL, we obtain $\frac{c_s}{2\pi R} \simeq 15$ kHz. Other characteristic frequency is $V_{\mathbf{E} \times \mathbf{B}}/L_p$ which we represent in Fig. ?? as a function of y which reveals itself to poloidally vary between 30 and 90 kHz. As the transition region is harder to find in the power-spectrum figure, we perform the fit at the startup position from 100 kHz (the characteristic frequency and the experimental position of the knee) to the last frequency data (300 kHz).

We have seen through the power-spectrum that different locations provide different slopes, which does not coincide with the experimental observations. This can be due to the different instabilities present at the LFS and HFS that may have different impact on the simulations and experiment (and therefore provide different slopes), but it requires further study.

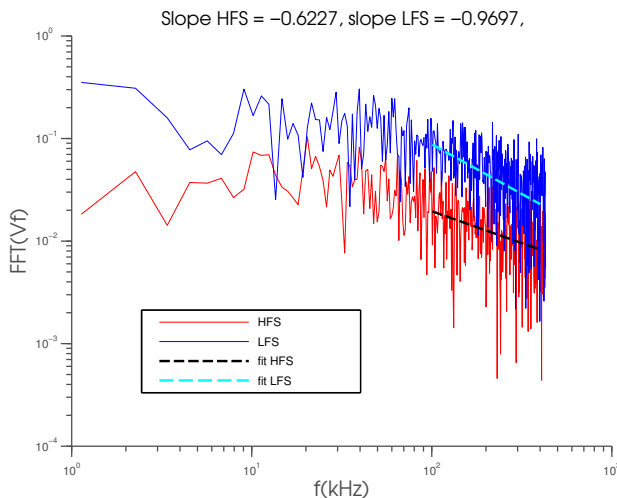


Figure 12: Power-spectrum at the HFS and LFS respectively for the floating potential V_f .

As before, the adimensionalized parameter that does

not take into account the SOL width difference between GBS simulations and experiment is η_e , where this difference is canceled out by the ratio L_n/L_T . From the simulations, we obtain a poloidal variation of η_e from 0.7 to 0.9, with an average value of $\bar{\eta}_e = 0.8$. Since the error bars from the fit provide an error of ± 0.05 , at the LFS $\eta_{e\text{GBS}} = 0.8 \pm 0.05$. The performed estimates with the experimental data are presented in table 2.

L_n	12.11
L_{T_e}	12.10
η_e	1.001
L_p	6.05

Table 2: Experimental results for L_n, L_T, η and L_p for ISTTOK in GBS units (1 GBS unit = 0.91 mm in SI units).

The experimental measurements were performed at the LFS, where it was found $\eta_{e\text{exp}} = 1.001$. The fundamental reason for this difference with the simulation values is that the actual scaling of the parameters L_n and L_T is not perfect as the SOL width is diminished in the GBS simulations, especially through the great observed poloidal variation. A simulation with the ISTTOK's SOL width value points to an increase of $\eta_{e\text{GBS}}$ but the results are not conclusive due to the destabilization provoked by such a small radial domain, mainly the major turbulence drive to the walls.

5. Conclusions

One of the main challenges of today's fusion program is to accurately predict the SOL dynamics and understand the physics behind it. It is a very rich domain, from the study of the plasma boundary conditions (where the plasma is lost to the divertor or limiter in this region) to the study of turbulence driven transport. SOL physics is what determines the boundary conditions for the plasma in the whole machine, regulating the power exhaust. In this work, we focus on the analysis of scrape-off layer dynamics on ISTTOK geometry, which has a single poloidal limiter and a large aspect ratio with a circular cross-section, and study the results provided from linear and non-linear simulations which are then compared to the existing experimental results.

GBS simulations allowed a discussion of the different modes present in the LFS and HFS through the non-linear tests described in section 3.4. It was observed a greater correlation between the electric potential and density at the HFS compared with the LFS, assessing the drift-wave character of the turbulence there. Performing the power-spectrum of the floating potential, we have identified different slopes at the HFS and LFS, which does not match the experimental results. This may be due to the different impact of the instabilities at those locations. The gradient removal hypothesis provided an L_p with the same behavior as seen on the non-linear simulations. It also pointed that at the LFS the inertial ballooning mode instability is responsible for the greatest linear growth rate, while at the HFS it is the inertial drift wave instability. Through a scan in \hat{s} we see that the value of magnetic shear is negligible

when it comes to assert the instabilities present on ISTTOK. The introduction of ionic temperature (through the introduction of a finite $\tau = \frac{T_i}{T_e}$) results on a small broadening of the poloidal range of the InDW branch. Looking at the experimental results, we have estimated a value of $L_p = 4.94$ at the LFS (in GBS units) while the non-linear show a value of $L_p = 14$. This was mainly due to the SOL width used in GBS simulations of $L_x = 50$, while at ISTTOK $L_x = 16$. Due to this fact, we look to the adimensionalized parameter η_e , where $\eta_{e_{GBS}} = 0.8$ and $\eta_{e_{ISTTOK}} = 1.0$, a relative error of 20 %.

Future extensions of this work include the study of non-linear simulations with different values of resistivity and magnetic shear in order to analyze the different instability branch (RBM) shown within the linear code and perform a study on the presence of plasma blobs in ISTTOK's SOL. Furthermore, in order to completely model ISTTOK's geometry, the parallel diffusion routine has to be ported to a poloidally symmetric configuration and the boundary conditions should include a real limiter with 12 graphite plates instead of a continuous poloidal plate. In order to address the analysis of future reactor relevant configurations, GBS simulations can be performed in a more complicated magnetic geometry (such as X-point geometry). Under study with this code is the simulation of plasma blobs [7], aspect ratio effects [23] and intrinsic toroidal rotation in the SOL which is relevant not only for ISTTOK (see for example [24]) but also for future tokamaks such as ITER.

Acknowledgements

This work results from the cooperation of two institutions - IPFN and CRPP. At IPFN, I would like to thank my supervisor Prof. Nuno Loureiro for the support since the beginning of the project and the choice of the extremely interesting topic and Prof. Carlos Silva, for supporting the project from the experimental point of view and providing valuable insight. At CRPP I found a new and outstanding way to study and do physics. It was a lifetime opportunity to be able to work in a fulfilling environment and with such amazing people. For this and much more, I thank my co-supervisor Prof. Paolo Ricci and Doctor Federico Halpern.

References

- [1] The World Bank. Fossil fuel energy consumption (% of total). Technical report, IEA Statistics, 2013.
- [2] J. Skea et al. *Making the Transition to a Secure Low-Carbon Energy System*. Routledge, 2010.
- [3] J. A. C. Cabral et al. Analysis of the ISTTOK plasma density profile evolution in sawtooth discharges by heavy-ion beam probing. *Plasma Physics and Controlled Fusion*, **38**(51), September 1995.
- [4] I. Langmuir et al. *Collected works: with contributions in memoriam, including a complete bibliography of his works*. Number v. 4 in Collected Works: With Contributions in Memoriam, Including a Complete Bibliography of His Works. Published with the editorial assistance of the General Electric Co. by Pergamon Press, 1961.
- [5] P. Ricci et al. Simulation of plasma turbulence in scrape-off layer conditions: the GBS code, simulation results and code validation. *Plasma Physics and Controlled Fusion*, **52**(124047), 2012.
- [6] P. Ricci et al. Langmuir probe-based observables for plasma-turbulence code validation and application to the TORPEX basic plasma physics experiments. *Physics of Plasmas*, **16**(5), 2009.
- [7] F. Halpern et al. Three-dimensional simulations of blob dynamics in a simple magnetized torus. *Physics of Plasmas*, **21**(2), 2014.
- [8] D. A. D'Ippolito et al. Convective transport by intermittent blob-filaments: Comparison of theory and experiment. *Physics of Plasmas*, **18**(060501), 2011.
- [9] G. Q. Yu et al. Two-dimensional modelling of blob dynamics in tokamak edge plasmas. *Physics of Plasmas*, **13**(4), 2006.
- [10] P. Ricci et al. Plasma turbulence in the scrape-off layer of tokamak devices. *Physics of Plasmas*, **20**(010702), November 2013.
- [11] S. Braginskii. Transport processes in a plasma. *Reviews of Plasma Physics*, **1**(6), 1965.
- [12] A. Zeiler et al. Nonlinear reduced Braginskii equations with ion thermal dynamics in toroidal plasma. *Physics of Plasmas*, **2134**(4), 1997.
- [13] C. Silva et al. Characterization of the poloidal asymmetries in the ISTTOK edge plasma. *Plasma Physics and Controlled Fusion*, **53**(8), 2011.
- [14] J. Loizu et al. Boundary conditions for plasma fluid models at the magnetic presheath entrance. *Physics of Plasmas*, **19**(122307), 2012.
- [15] P.C. Strangeby. *The plasma boundary of magnetic fusion devices*. Institute of Physics Pub, Bristol Philadelphia, 2000.
- [16] A. Masetto et al. Turbulent regimes in the tokamak scrape-off layer. *Physics of Plasmas*, **20**(9), 2013.
- [17] A. Zeiler et al. Three-dimensional fluid simulations of tokamak edge turbulence. *Physics of Plasmas*, **3**(8), 1996.
- [18] J. F. Drake et al. Nonlinear self-sustained drift-wave turbulence. *Physical Review Letters*, **75**(23), Dec 1995.
- [19] B. Scott. Three-dimensional computation of drift Alfvén turbulence. *Plasma Physics and Controlled Fusion*, **39**(10), 1997.
- [20] B. D. Scott. Drift wave versus interchange turbulence in tokamak geometry: Linear versus nonlinear mode structure. *Physics of Plasmas*, **12**(062314), 2005.
- [21] J. F. Drake et al. Nonlinear self-sustained drift-wave turbulence. *Physical Review Letters*, **75**(4), 1995.
- [22] C. Silva et al. Overview of recent ISTTOK results. *AIP Conference Proceedings*, **996**(1), 2008.
- [23] S. Jolliet et al. Aspect ratio effects on limited scrape-off layer plasma turbulence. *Physics of Plasmas*, **21**(2), 2014.
- [24] C. Silva et al. Characterization of geodesic acoustic modes in the ISTTOK edge plasma. *Plasma Physics and Controlled Fusion*, **51**(8), 2009.